Impacts of Idealized Air–Sea Coupling on Madden–Julian Oscillation Structure in the Superparameterized CAM

JAMES J. BENEDICT AND DAVID A. RANDALL

Department of Atmospheric Science, Colorado State University, Fort Collins, Colorado

(Manuscript received 3 January 2011, in final form 16 March 2011)

ABSTRACT

Air–sea interactions and their impact on intraseasonal convective organization are investigated by comparing two 5-yr simulations from the superparameterized Community Atmosphere Model version 3.0 (SP-CAM). The first is forced using prescribed sea surface temperatures (SSTs). The second is identical except that a simplified oceanic mixed-layer model is used to predict tropical SST anomalies that are coupled to the atmosphere. This partially coupled simulation allows SSTs to respond to anomalous surface fluxes.

Implementation of the idealized slab ocean model in the SP-CAM results in significant changes to intraseasonal convective variability and organization. The more realistic treatment of air–sea interactions in the coupled simulation improves many aspects of tropical convection on intraseasonal scales, from the relationships between precipitation and SSTs to the space–time structure and propagation of the Madden–Julian oscillation (MJO). This improvement is associated with a more realistic convergence structure and longitudinal gradient of SST relative to MJO deep convection. In the uncoupled SP-CAM, SST is roughly in phase with the MJO convective center and the development of the Kelvin wave response and boundary layer convergence east of the convective center is relatively weak. In the coupled SP-CAM, maxima in SST lead maxima in MJO convection by $\frac{1}{4}$ cycle. Coupling produces warmer SSTs, a stronger Kelvin wave response, enhanced low-level convergence, and increased convective heating ahead (east) of the MJO convective center. Convective development east of the MJO precipitation center is more favorable in the coupled versus the uncoupled version, resulting in more realistic organization and clearer eastward propagation of the MJO in the coupled SP-CAM.

1. Introduction

The Madden–Julian oscillation (MJO; Madden and Julian 1971) is the dominant feature of the tropical atmosphere on intraseasonal time scales. The MJO is characterized by multiscale interactions within and between a number of different components of the atmosphere, ocean, and land systems [see Lau and Waliser (2005) and Zhang (2005) for reviews]. The complexity of these interactions makes it difficult to achieve a full understanding of the MJO, and accurately simulating the MJO remains a formidable challenge (Lin et al. 2006).

To capture the full detail of MJO disturbances, general circulation models (GCMs) must accurately represent multiscale and subgrid-scale cloud processes, interactions of moist convection and dynamics on a wide range of space–time scales, exchanges of heat and moisture between the atmospheric boundary layer and ocean surface, and tropical–extratropical connections. Modeling issues related to convection, radiation, and microphysical parameterizations; air–sea coupling; and horizontal and vertical grid resolution must also be addressed. Faced with this daunting task and our lack of understanding of MJO mechanisms, it is no surprise that many GCMs have a poor representation of intraseasonal variability (Slingo et al. 1996, 2005; Lin et al. 2006; Kim et al. 2009).

The present study investigates interactions between the atmosphere and ocean systems and their impact on the simulated MJO in a superparameterized (SP) GCM. We use the SP version of the National Center for Atmospheric Research (NCAR) Community Atmosphere Model (CAM, version 3.0; Collins et al. 2006), which has been shown to simulate the MJO well (Khairoutdinov et al. 2008; Benedict and Randall 2009; Zhu et al. 2009). The SP-CAM replaces conventional boundary layer, moist convection, and cloud parameterizations with a cloud-resolving model (CRM) embedded in each CAM

Corresponding author address: Jim Benedict, Department of Atmospheric Science, Colorado State University, Fort Collins, CO 80523–1371.
E-mail: jim@atmos.colostate.edu

DOI: 10.1175/JAS-D-11-04.1

grid cell (Khairoutdinov and Randall 2001). Intraseasonal variability in the SP-CAM increases markedly over the standard CAM, the variability of which, like that of many GCMs, remains unrealistically weak (Lin et al. 2006; Khairoutdinov et al. 2008). Important features that are fundamental to the MJO, such as the tilted convective heating and moistening structures and processes related to advective drying following deep convection, are well simulated in the SP-CAM (Benedict and Randall 2009).

To examine the role of air–sea fluxes on the MJO, we couple the SP-CAM to a simplified slab ocean model that allows for a more realistic treatment of sea surface temperatures (SSTs) and their interaction with the atmosphere. Nearly all previous studies that use SP-GCMs to examine intraseasonal variability have forced the simulation with prescribed SSTs (e.g., Khairoutdinov and Randall 2001; Khairoutdinov et al. 2005, 2008; Zhu et al. 2009; Benedict and Randall 2009; Thayer-Calder and Randall 2009). Historically, parameterizations are tuned such that selected climate features are optimally represented when the atmospheric component of the model is forced by prescribed SSTs. In many cases, however, these tuning schemes involve a cancellation of errors. When the atmospheric component is coupled to a dynamic ocean model, the errors may no longer cancel and the depiction of the climate can become less realistic (e.g., Hack et al. 2006; Stan et al. 2010).

The first studies in which an SP-GCM is coupled to an ocean model include Benedict (2009), Stan et al. (2010), and DeMott et al. (2011). The present study is an extension of the work presented in Benedict (2009), who coupled the SP-CAM to an idealized slab ocean model. Stan et al. (2010) and DeMott et al. (2011) are the only studies thus far that have coupled an SP-GCM to a full-physics ocean model. Those authors examined 22 yr of simulated data from an untuned SP version of the NCAR Community Climate System Model (version 3; SP-CCSM) and found improvement over the standard CCSM3 for mean state, interannual, and subseasonal climate features. The SP-CCSM results show a more realistic MJO during the boreal winter and during the boreal summer when it interacts with the Asian monsoon, suggesting that a more natural representation of air–sea interaction improves intraseasonal variability in SP-GCMs, as has been previously demonstrated with many conventional GCMs (Inness and Slingo 2003; Sperber 2004; Rajendran and Kitoh 2006). One drawback of coupling a GCM to a full-physics ocean model is that SSTs can deviate strongly from observations. Stan et al. (2010) found mean Indo-Pacific SST biases of 1–2-K cooling in the SP-CCSM compared to observations, and these biases must ultimately influence wind and precipitation patterns on a variety of space and time scales. The present study complements the work of Stan et al. (2010) and DeMott et al. (2011) but is aimed at isolating the impact of air–sea interactions on the MJO in a framework in which the mean atmospheric and oceanic states of the coupled and uncoupled simulations remain very similar through the use of a slab ocean model that is constrained to produce a basic state close to climatology.

In section 2 we provide a historical view of selected studies that have investigated air–sea interactions and their impact on the MJO. We review the slab ocean model as well as the simulation and validation datasets in section 3. Section 4 contains a brief overview of statistical analysis methods used in this study. We present our results in section 5, followed by a discussion and summary in section 6.

2. A brief review of air–sea interaction and its connection to the MJO

Numerous observational, theoretical, and modeling studies have demonstrated that robust interactions between the atmospheric and oceanic mixed layers occur on intraseasonal space–time scales. One of the first observational studies to highlight this topic was reported by Krishnamurti et al. (1988), who discovered that the ocean supplies the atmosphere with moisture for sustained cumulus heating primarily through surface latent heat fluxes that are regulated by intraseasonal boundary layer wind fluctuations. Krishnamurti et al. (1988) also contended that air–sea coupling would be a necessary component of future GCMs if a full understanding of the MJO is to be achieved. Using data from the Tropical Ocean–Global Atmosphere (TOGA) Tropical Atmosphere–Ocean (TAO; Hayes et al. 1991) buoy array, Zhang and McPhaden (1995) investigated relationships among ocean surface temperature, wind, and evaporation and found a 10-day lag between atmospheric forcing from surface winds and the oceanic response. Lau and Sui (1997) examined TOGA Coupled Ocean–Atmosphere Response Experiment (TOGA COARE; Webster and Lukas 1992) data and demonstrated that intraseasonal surface shortwave fluxes, which are modulated by deep convection, add to evaporative fluxes both constructively and destructively depending on the MJO phase. Jones and Weare (1996) used European Centre for Medium-Range Weather Forecasts (ECMWF) surface analyses and International Satellite Cloud Climatology Project (ISCCP) brightness temperatures to conclude that the coherent eastward propagation of MJO convection is associated with low-level moisture convergence but weak evaporative fluxes to the east of the convective center.

Further investigation revealed that strong surface evaporation lags deep convection by only a few days in the western Pacific but potentially more than a week over the Maritime Continent and Indian Ocean (Zhang 1996; Hendon and Glick 1997; Shinoda et al. 1998). Fluctuations of surface shortwave radiation were found to be dominant over evaporation for the surface energy balance in the Indian Ocean, with the two components contributing equally in the western Pacific (Shinoda et al. 1998). The combined effects of insolation and surface latent heat flux drive intraseasonal SST fluctuations of about 0.2°–0.3°C on average (e.g., Lau and Sui 1997; Shinoda et al. 1998).

Summarizing the cumulative observational evidence [see reviews in Zhang (2005) and Hendon (2005)], the current paradigm linking air–sea interactions with the MJO suggests that strong insolation and weak evaporation occur during the convectively suppressed MJO phase because of widespread clear skies and easterly wind stress anomalies that oppose the westerly mean state flow. Heat fluxes into the ocean and shoaling of the oceanic mixed layer result in peak SSTs approximately 10 days prior to maximum convective intensity. As SSTs peak and the atmosphere becomes unstable, developing cumuli begin to decrease surface insolation. Incident shortwave radiation at the surface reaches a minimum, low-level westerlies strengthen, and SSTs decline rapidly around the time of maximum MJO precipitation. Two to eight days later, westerly wind stress anomalies are most intense and coincide with the strongest evaporative fluxes. SSTs reach a minimum about 10 days after deep convection because of the combined effects of strong evaporation and minimal insolation at the surface, and a deepening oceanic mixed layer that entrains cooler subsurface waters. The return of positive surface insolation anomalies and reduced surface winds gradually warms SSTs and shallows the oceanic mixed layer, signaling the beginning of the next intraseasonal convective episode.

Several theoretical studies have investigated the role that air–sea interactions play in MJO representation. The wind-induced surface heat exchange mechanism (WISHE; Emanuel 1987; Neelin et al. 1987) states that winds resulting from an equatorial heat source will generate enhanced (weakened) evaporation to the east (west) of the heating given a background easterly flow regime. The enhanced air–sea fluxes ahead of the main heating would increase low-level moist entropy, which would then be redistributed through the troposphere by developing convection. Thus, deep convective heating is shifted toward warm anomalies in a quasi-equilibrium system and eddy available potential energy (EAPE) is generated (Emanuel 1994). Although observational evidence does not support the original theory (e.g., Jones and Weare 1996), modified versions of WISHE might apply to the MJO in a nonlinear sense (e.g., Maloney and Sobel 2004). In particular, the positive covariance between precipitation and evaporation may be necessary to destabilize the MJO in some GCMs (Sobel et al. 2008; Maloney et al. 2010), and this destabilization can occur in a low-level westerly regime, as observed.

Wang and Xie (1998) constructed a simple coupled ocean–atmosphere model, which produced a moist Kelvin mode reminiscent of the observed MJO. Their Kelvin mode favors the generation of EAPE and its conversion to eddy kinetic energy via two mechanisms. The first involves an overlap of shallow convective heating with positive temperature anomalies, while the second requires a covariance between SSTs and low-level temperatures. The first mechanism alone cannot produce unstable Kelvin mode growth, such that a covariance between warm SSTs and low-level temperatures (lower surface pressures) is necessary for disturbance strengthening (Wang and Xie 1998). The exact mechanism of disturbance growth is unclear, and applicability to the MJO remains uncertain considering the differences between moist Kelvin modes and the MJO.

Until the mid-1990s, GCM-based studies of MJO maintenance and eastward propagation primarily focused on the atmosphere and not the ocean (Emanuel 1987; Lau et al. 1989; Hu and Randall 1994). One of the first numerical modeling studies to investigate air–sea coupling impacts on the MJO was Flatau et al. (1997), who examined how longitudinal SST gradients affect MJO phase speed in an aquaplanet GCM. Those authors demonstrated that weak surface evaporation and strong insolation ahead of deep convection warm SSTs and provide the increased surface moist entropy required to fuel new convection to the east, resulting in more coherent eastward propagation of the MJO. Flatau et al. (1997) assert that the MJO is a coupled atmosphere–ocean phenomenon but fall short of fully explaining how interactions among convection, radiation, evaporation, and SSTs improve the MJO depiction in their model. Waliser et al. (1999) greatly advanced the scope and understanding of how air–sea interactions modify the MJO. They compared two GCM simulations, one forced by prescribed SSTs (‘‘control’’) and a second in which SSTs were allowed to deviate from their prescribed values in the presence of surface flux anomalies (‘‘coupled’’). SST fluctuations driven by air–sea interactions in the coupled GCM increased meridional moisture convergence associated with frictional wave conditional instability of the second kind (CISK) (Wang 1988) to the east of the convective center. The greater moisture availability ultimately intensified the disturbance and/or

maintained it against dissipation while promoting eastward propagation (Waliser et al. 1999).

Improvement in the structure and propagation of the MJO with air–sea coupling has been documented for many other GCMs, including earlier versions of the CAM (Sperber 2004), the Hadley Centre GCM [i.e., the atmospheric component of the third climate configuration of the Met Office Unified Model (HadAM3); Inness and Slingo 2003], the European Centre Hamburg Model GCM (ECHAM4; Kemball-Cook et al. 2002; Sperber et al. 2005), the Meteorological Research Institute (MRI) GCM (Rajendran and Kitoh 2006), and the Australian Bureau of Meteorology Centre's atmospheric GCM version 3.0 (BAM3; Marshall et al. 2008). Coupling a GCM to an idealized or full-physics ocean model generally results in the formation of a transient longitudinal gradient of SST, such that positive (negative) SST anomalies form east (west) of MJO convection (e.g., Waliser et al. 1999). Convective development (suppression) is then favored to the east (west) of the MJO convective center, promoting eastward propagation. Hypotheses linking the more realistic SST gradients with improved MJO propagation often invoke frictional wave-CISK arguments in which the warm SST anomalies east of the convection center support enhanced meridional convergence, which destabilizes the atmosphere and induces convective development (Waliser et al. 1999; Kemball-Cook et al. 2002; Rajendran and Kitoh 2006). Zhang et al. (2006) emphasize the importance of accurately simulating the mean state in coupled GCM studies of the MJO. Those authors caution that although air–sea coupling generally improves the MJO in their analyses, inconsistencies between simulations indicate that coupling may not improve the MJO in every model. Evidence from many conventional GCM studies strongly suggests that, while not critical for its existence, air–sea coupling makes MJO representation more realistic.

3. Data sources

We analyze two SP-CAM simulations to investigate the effects of simplified ocean–atmosphere coupling. The host GCM for both simulations is CAM3.0, which has a horizontal grid resolution is 2.8° × 2.8°, 30 levels with a 3.6-hPa top, and a time step of 30 min. The CRMs embedded into each CAM grid cell have 32 columns oriented north–south, a horizontal resolution of 4 km, 28 levels collocated with the lowest CAM levels, and a time step of 20 s. Additional details of the SP-CAM configuration are available in Khairoutdinov et al. (2008) and references therein. The first simulation dataset is a 5-yr segment taken from the end of an Atmospheric Model Intercomparison Project (AMIP)-style run described in Benedict and Randall (2009). It spans 1 September 1999–31 August 2004 and will be referred to as the ''control'' run (CTL). The second simulation is identical to the first except for interactive tropical SSTs. A simplified mixed-layer ocean model is used to calculate prognostic SST anomalies that are coupled to the atmosphere. We call this second simulation the ''slab ocean model'' run (SOM). SSTs in the SOM are allowed to deviate slightly from their prescribed values when anomalous surface fluxes exist. Unlike the CTL, the ocean in the SOM can respond to anomalous surface fluxes.

The idealized ocean mixed-layer model implemented in the SOM is an adaptation of (1) in Waliser et al. (1999):

$$\frac{dT'}{dt} = \frac{F'}{\rho C H} - \gamma T'. \tag{1}$$

Here T' is the SST departure from the monthly mean (linearly interpolated to daily mean) observed SST, F' the departure of the total net surface flux from its climatological value, ρ the water density, C the specific heat of water, H the climatological oceanic mixed-layer depth, and γ a damping coefficient. Climatological values of H and net surface flux represent smoothed seasonal cycles at daily temporal resolution. Net surface flux climatological values used in (1) are computed directly from the CTL simulation and smoothed by retaining only the mean and first three harmonics of the seasonal cycle. Although Waliser et al. (1999) fix the value of H at 50 m, in (1) the mixed-layer depth is space and time dependent as described by Monterey and Levitus (1997). We use only the mean and first three harmonics of the seasonal cycle of H and pass this cycle through a 1–2–1 temporal filter to prevent negative values where shoaling occurs rapidly in time. The annual mean of the smoothed H values is about 30–35 m in the warm pool region but can drop to less than 10 m around the Maritime Continent. The γ parameter represents the time scale for SST perturbations to return to zero or, alternatively, the time scale for SSTs to return to their prescribed values. As in Waliser et al. (1999), we set $\gamma = (50 \text{ day})^{-1}$ in the SOM to match the approximate decorrelation time scale of tropical intraseasonal phenomena (Hendon and Salby 1994). The $\gamma T'$ term in (1) also maintains a realistic SST climatology.

The MJO has a strong sensitivity to the mean state, such that small changes in background conditions can have an impact on the character of intraseasonal disturbances (Hendon and Salby 1994; Inness and Slingo 2003). It is therefore important to limit differences in the climatological states between the CTL and SOM

simulations so that changes in the MJO between the two runs can be more directly attributed to air–sea interactions on intraseasonal scales. The SST fluctuations caused by strong surface fluxes at middle and high latitudes can be large and may potentially alter the climatological dynamical fields. Because we are interested in the effects of air–sea interactions on the MJO and wish not to significantly alter the mean state of the model, we only apply the slab ocean model equatorward of 26°. A Hann weighting function is applied from 12° (1.0 weight) to 26° (0.0 weight), and the slab ocean model is fully active within 12° of the equator. Poleward of 26°, SSTs exactly equal their prescribed values.

We compare the simulation results to several observation-based datasets. To facilitate comparison, all data sources are daily averaged and linearly interpolated to a 2.5° horizontal grid and 27 vertical levels between 1000 and 100 hPa. Except for precipitation, outgoing longwave radiation (OLR), and SST, all observation-based fields are obtained from the interim ECMWF Re-Analysis dataset (ERA-Interim, hereafter abbreviated as ERAI; Berrisford et al. 2009). Like its predecessor, the 40-yr ECMWF Re-Analysis (ERA-40; Uppala et al. 2005), ERAI is a by-product of surface and satellite measurements blended with short-term model forecasts. ERAI benefits from full data coverage in space and time but is subject to the same deficiencies as ERA-40—namely, a strong dependence on model physics and parameterizations where measurements are sparse. We use ERAI in this analysis because it covers the selected time range (1999–2004) and exhibits several notable improvements over the ERA-40 dataset (see Simmons et al. 2006; Berrisford et al. 2009). Overall, ECMWF reanalyses are well suited for the study of mesoscale to planetary-scale tropical weather features (Straub and Kiladis 2003; Sperber 2003; Kiladis et al. 2005; Benedict and Randall 2007).

Observed rainfall data are taken from the Global Precipitation Climatology Project (GPCP; Adler et al. 2003) and OLR data are derived from the National Oceanic and Atmospheric and Administration's (NOAA's) suite of polar-orbiting satellites (Liebmann and Smith 1996). We use version 2 of NOAA's Optimum Interpolation SST (OISST2; Reynolds et al. 2002) dataset for ocean surface temperatures. We note that the OISST2 product may not fully capture rapid SST changes in space and/or time because of its large spatial decorrelation scale and weekly time resolution (Chelton and Wentz 2005).

4. Methods

We employ a number of statistical analysis methods to highlight intraseasonal variability, clarify relationships between convection and dynamics, and reveal MJO structure. Unlike the results shown in Benedict and Randall (2009), which are based on composites of many MJO events, the limited time span of the simulation segments used here (1825 days) requires an alternative analysis approach to ensure that results are statistically robust and meaningful. Outlined below is a selection of the primary methods used to examine the impacts of air–sea coupling on the SP-CAM.

a. Decile averaging

We assess the most basic relationships between convection (as measured by precipitation) and other fields by constructing decile histograms. These plots are generated by first ranking precipitation values for all space and time points within a specified domain. We choose a domain that includes all days and ocean grid points within the region in which the MJO is most active: 10°S–10°N, 60°E–180°. The ranked precipitation values are then divided into 10 bins (deciles), and other selected variables can be averaged based on these precipitation deciles. For example, one can compute the average SST corresponding to the driest 10% of rainfall occurrences, the wettest 10% of rainfall occurrences, and deciles in between. The decile histograms only indicate simple associations between convection and other variables and contain no information about time or space dependencies.

b. Zonal wavenumber–frequency analysis

It is often useful to partition the total variability of a selected field into its zonal wavenumber and frequency components. We utilize this statistical approach (Hayashi 1982; Wheeler and Kiladis 1999) to compare several features of the simulation and observation datasets. Zonal wavenumber–frequency analysis effectively highlights the spectral power for different wave types—that is, the magnitude of variability contained within specific zonal wavenumbers and frequencies relative to a background variability—as well as the power ratio of westward- to eastward-propagating wave features. We use such methods to determine differences among the MJO spectral signals between the CTL and SOM.

c. Lag correlation

We use lag correlation methods to deduce the strength and direction of linear relationships between two variables in time and/or space. The lag correlation technique indicates the extent to which two variables are linearly related but provides no information regarding (a) how amplitude changes in the two variables are linearly related and (b) the nonlinear relationship between variables. Statistical significance of the correlation between two variables is computed using the t test statistic

$t = r(N^* - 2)^{1/2}(1 - r^2)^{-1}$. Here, r is the correlation coefficient and the effective sample size is $N^* = N(1 - r_1 r_2)(1 + r_1 r_2)^{-1}$, where N is the number of available time steps and r_1 and r_2 are lag-1 autocorrelations at the two spatial points we are interested in correlating (Bretherton et al. 1999). For the bandpass-filtered data used in this study, $N = 1466$ (reduced from 1825 because time series ends are tapered to reduce spurious spectral signals) and $N^* \sim 20$–30 for variables in the Indo-Pacific region.

d. Linear regression

Regression techniques capture the relationship between fluctuations of one variable with changes in another. All regression plots shown in this paper display the linear, time-lagged association of a dependent variable to an index designed to capture convective fluctuations of the MJO. We choose this index to be 20–100-day filtered precipitation that has been standardized. Statistical significance is computed using the correlation coefficients and t test statistics from the equations in section 4c.

5. Results

Because the MJO has a strong sensitivity to the mean state in which it operates (e.g., Inness and Slingo 2003), it is important to verify that the climatological settings in the two versions of the SP-CAM are similar. Figure 1 displays annual mean state differences in 850-hPa zonal wind (U850), precipitation, and SST [the reader is referred to Benedict and Randall (2009) for additional SP-CAM climate plots]. We analyze the annual mean rather than the boreal winter mean because of the short time record (1999–2004). Figures 1a and 1b indicate that annual mean differences between CTL and SOM are generally less than 1 m s^{-1} for U850 and less than 1 mm day^{-1} for precipitation, respectively. For these two variables, pattern correlations are greater than 0.98 and normalized root-mean-square errors (NRMSEs) are less than 0.08.[1] This indicates that the climatological spatial structures are very similar and the cumulative biases are less than 10% of a representative standard deviation from CTL. SST mean state differences (Fig. 1c) are typically 0.1 K or less away from the coastlines, where larger differences are likely due to an increased sensitivity of SST on surface flux anomalies for shallow oceanic mixed layer depths [see (1)]. Overall, the annual mean state differences between CTL and SOM are small, and MJO differences between the two runs can be mainly attributed to changes in air–sea interactions.

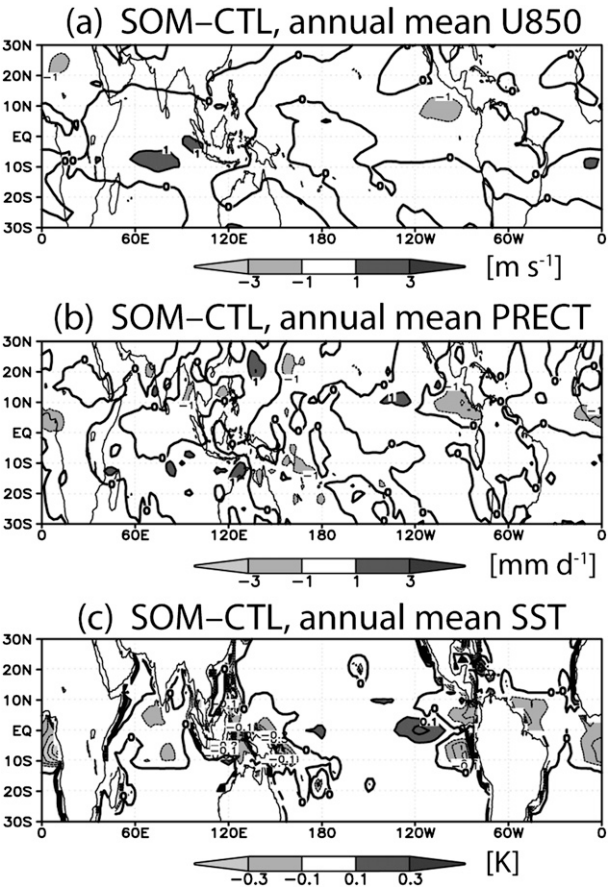

FIG. 1. Annual mean state differences (SOM − CTL) of (a) 850-hPa zonal wind, (b) precipitation, and (c) SST.

All-season variance fields of MJO-filtered U850 and precipitation are shown in Figs. 2 and 3 , respectively. We choose a spectral domain of zonal wavenumbers +1 to +6, signifying eastward-propagating disturbances, and periods of 20–100 days for the filtering process. For clarity, we show variance values only equatorward of 20°. Both versions of the SP-CAM generally overestimate MJO variance, with the exception of near-equatorial precipitation in the Indian and western Pacific regions. Figure 2c indicates that climatological MJO U850 variance in the SOM is generally larger than in both the CTL (Fig. 2b) and observations (Fig. 2a). Some improvement of MJO precipitation variance is noted in the SOM, however. Figure 3c displays a strong reduction in MJO precipitation variance in the South Pacific convergence zone and increased variance in the equatorial eastern Indian Ocean for the SOM compared to the CTL (Fig. 3b). There is no clear explanation as to why biases

[1] The domain used for pattern correlation and NRMSE calculations is 20°S–20°N, 60°E–100°W. The RMSEs are normalized by the average of the standard deviations from each spatial point in the domain, taken from the CTL.

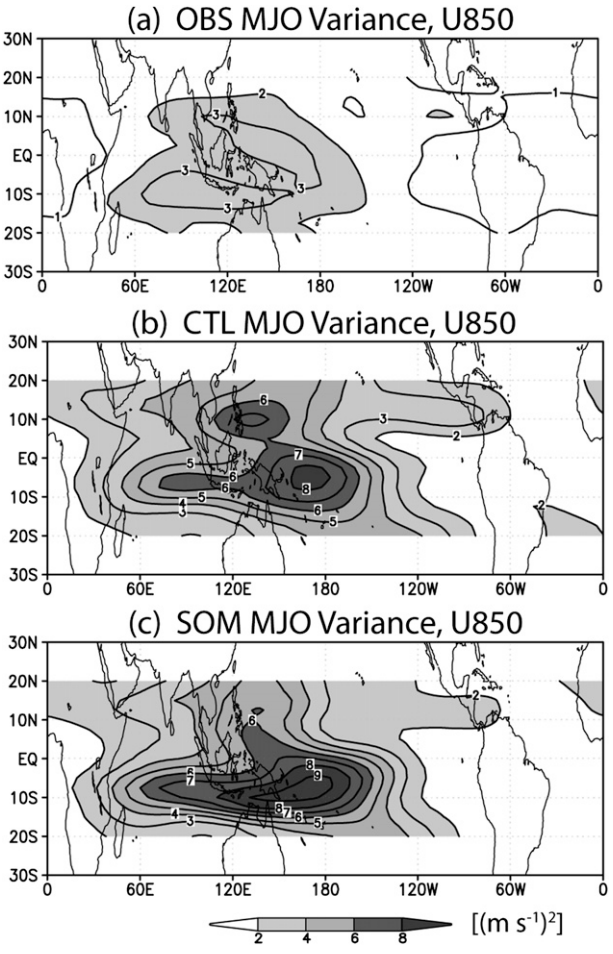

FIG. 2. All-season MJO-filtered variance of 850-hPa zonal wind for (a) ERAI, (b) CTL, and (c) SOM. The MJO filter retains eastward-propagating disturbances with zonal wavenumbers 1–6 and periods of 20–100 days.

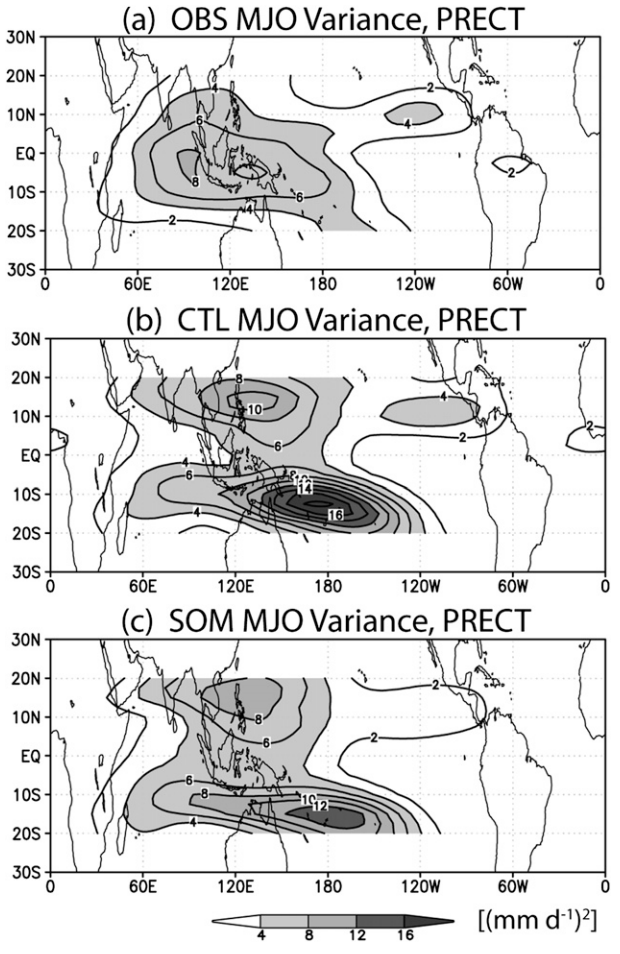

FIG. 3. As in Fig. 2, but for precipitation.

in MJO U850 variance worsened yet precipitation variances improved in the SOM.

Net surface fluxes drive SST changes in SOM [see (1)]. All-season MJO-filtered variance of net surface fluxes from (a) ERAI, (b) CTL, and (c) SOM are displayed in Fig. 4. Both versions of the SP-CAM underestimate (overestimate) net surface flux variance along (off) the equator, although it is important to note that fluxes from ERAI are highly parameterized. Despite a generally modest difference in annual mean net surface flux between the two simulations (not shown; ~15% or less in the equatorial Indo-Pacific region), there is a sizable reduction (~25%–33%) of net surface flux variance in SOM compared to CTL. This reduction is expected given the negative feedback between SSTs and net fluxes in the slab ocean model. The decreased net surface flux variance is associated with an increase in all-season 20–100-day bandpass-filtered SST variance in SOM relative to CTL (not shown), suggesting that the phase relationships between SST and surface fluxes relative to MJO deep convection are different in the two simulations.

We examine the relationship between 20–100-day bandpass-filtered precipitation and SSTs in Fig. 5. We caution that only limited interpretation of the decile profiles is possible in the context of the MJO because the plots do not contain any information regarding space or time dependencies. For example, we can assume that deciles 1–3 (8–10) correspond to the MJO phase in which convection is strongly suppressed (active), but the relationship for intermediate deciles is less clear. Figure 5 highlights a flawed relationship between convection and SSTs in the CTL, where SSTs increase steadily with increasing rain rate. The opposite is true for both the SOM and observations. We note that the OISST2 dataset provides weekly (linearly interpolated to daily) SST averages, suggesting that the anomaly magnitudes of the observed SSTs shown may be underestimated. Overall,

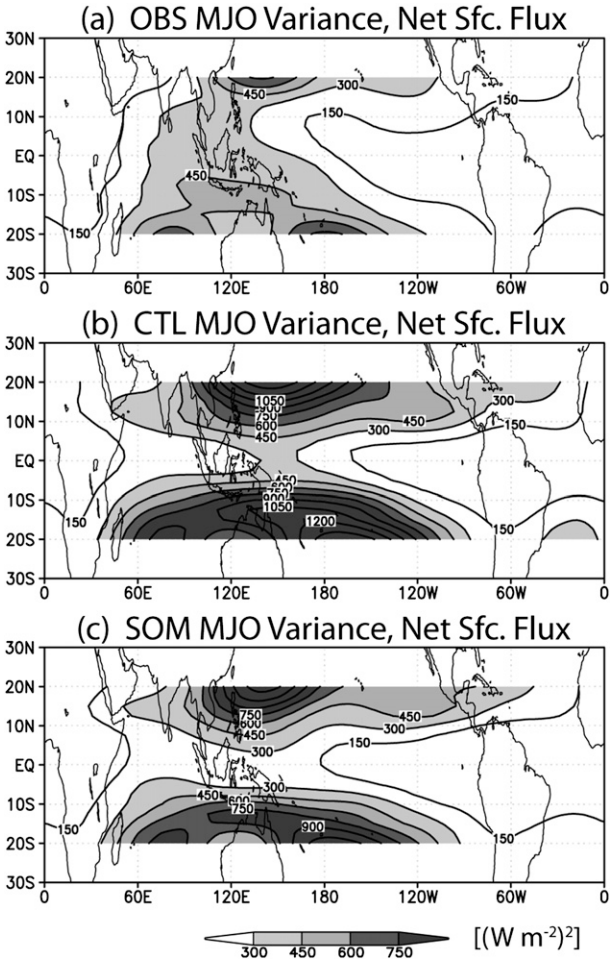

FIG. 4. As in Fig. 2, but for net surface flux.

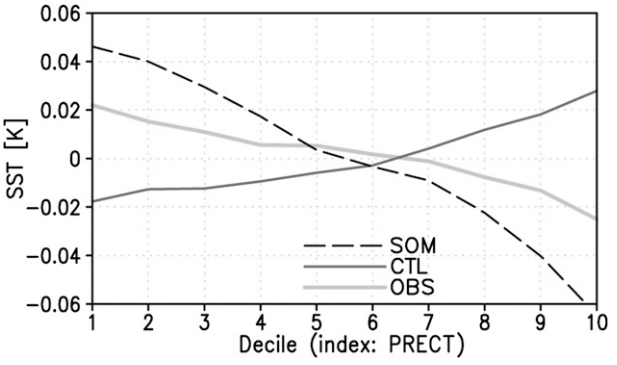

FIG. 5. Bandpass-filtered (20–100 days) SST binned based on deciles of bandpass-filtered precipitation for all seasons and all ocean grid points within the region 10°S–10°N, 60°E–180°. We use OISST2 for the observed SST field.

Fig. 5 indicates that the processes by which convection modulates SSTs are more realistic in the SOM compared to the CTL.

We present zonal wavenumber–frequency diagrams of tropical precipitation for (a) observations, (b) CTL, and (c) SOM in Fig. 6. The antisymmetric (ASYM) and symmetric (SYM) raw spectra (first and third rows, respectively) are the base-10 logarithm of the summation of power from 15°S to 15°N. Overall, the spectra from CTL and SOM appear to be qualitatively similar, but important differences exist. The significant portion of the SYM spectra (i.e., raw power divided by a smoothed background; see Wheeler and Kiladis 1999) at the bottom of Fig. 6 suggests that there is a slightly clearer Kelvin wave signal in SOM. Equatorial Rossby waves have shifted to higher frequencies in SOM as well, which is in better agreement with observations (Fig. 6, bottom row). Although there is a slight expansion toward higher frequencies in the MJO spectral region, the signal-to-noise ratio of MJO disturbances is improved in SOM.

An important diagnostic drawn from spectral analysis is the ratio of raw power values between westward- and eastward-propagating features (Lin et al. 2006; Kim et al. 2009). Most GCMs have difficulty in capturing the correct east–west power ratio of the MJO signal (Lin et al. 2006), but it has been shown that these ratios in the SP-CAM are comparatively closer to observations (Kim et al. 2009). In Table 1 we present east–west power ratios within a chosen MJO spectral domain[2] for the observations, CTL, and SOM. Although still falling short of the observed ratio values, the SOM results show a 25%–35% increase in east–west power ratio for convective and dynamic variables compared to CTL. This demonstrates that the implementation of the slab ocean model in the SP-CAM is associated with clearer eastward MJO propagation and a reduced standing wave signal.

Improved coherence of the MJO signal in the SOM can also be seen through lag correlation analysis. Figure 7 displays SST[3] lag correlated with a standardized precipitation index at each longitude. Both variables have been averaged between 10°S and 10°N. We also tested averaging of 15°S–5°N and 5°S–5°N and found that our conclusions do not change based on the selected latitude range. Dark (light) shading represents positive (negative) correlation values above the 95% significance threshold. The effects of the slab ocean model are immediately apparent. In nature (Fig. 7a), warm SSTs depicted by

[2] For all variables, the frequency domain includes periods of 32–96 days. For OLR and precipitation, we compare the accumulated raw power in zonal wavenumbers +1 and +2 (propagation to east) to zonal wavenumbers −1 and −2 (propagation to west). For U850, we compare zonal wavenumber +1 to −1.

[3] For the remaining figures and discussion in this paper, all variables have had the mean and first three harmonics of their seasonal cycle removed and have been bandpass filtered (20–100 days) prior to correlation or regression calculations.

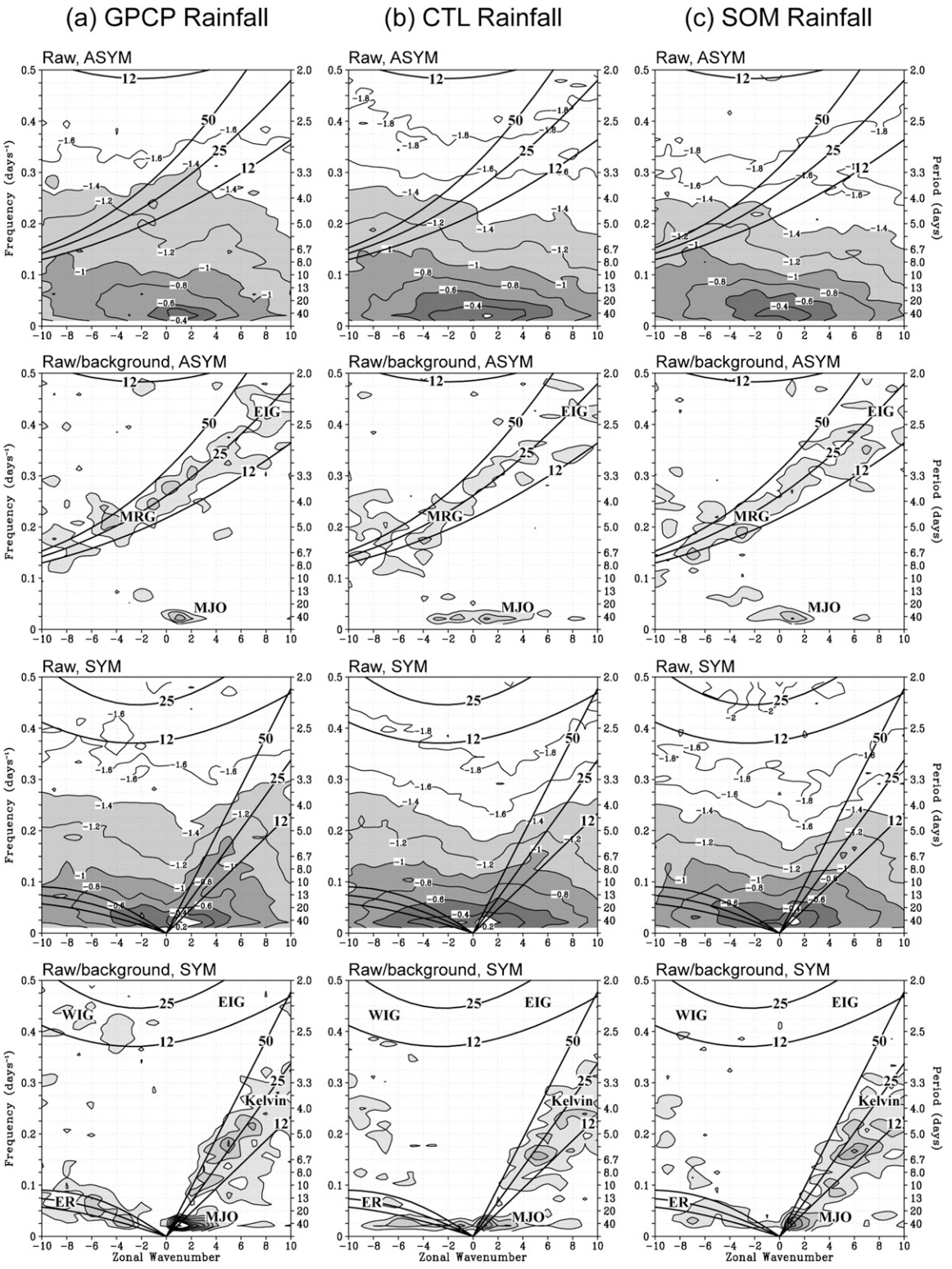

FIG. 6. Frequency–zonal wavenumber power spectra of precipitation from (a) GPCP, (b) CTL, and (c) SOM. (top to bottom) Raw power for antisymmetric (ASYM) components, raw power divided by a smoothed background power for ASYM components (hereafter, the signal-to-noise ratio), raw power for symmetric (SYM) components, and signal-to-noise ratio for SYM components. Raw power values are the base-10 logarithm of the summation of power from 15°S to 15°N. Contour intervals for signal-to-noise ratio plots are 0.2 between 1.1 and 2.5 and 0.5 above, with identical shading intervals between 1.1 and 2.5 and no shading above 2.5. Superimposed are dispersion curves for equivalent depths of 12, 25, and 50 m for equatorial Rossby (ER), Kelvin, westward and eastward inertio-gravity (WIG and EIG, respectively), and mixed Rossby–gravity (MRG) waves and the MJO. Negative (positive) zonal wavenumbers correspond to westward (eastward)-moving disturbances.

TABLE 1. Power ratios of eastward- to westward-propagating equatorial wave features within the MJO spectral domain. For all variables, the frequency domain includes periods of 32–96 days. For OLR and precipitation, we compare the accumulated raw power in zonal wavenumbers +1 and +2 (propagation to east) to zonal wavenumbers −1 and −2 (propagation to west). For U850, we compare zonal wavenumber +1 to −1.

	Precipitation	OLR	U850
Observations	2.7	3.1	5.9
CTL	1.3	1.7	2.6
SOM	1.7	2.1	3.5

solid contours and dark shading lead peak MJO precipitation by 1–2 weeks in the Indo-Pacific region, while cool SSTs lag the heaviest rainfall by about 1 week (Kawamura 1988; Inness and Slingo 2003). A strong resemblance to this pattern is seen in the SOM results (Fig. 7c) with the exception that the time between the leading maximum and trailing minimum correlations is shorter in the SOM relative to nature, particularly near the Maritime Continent where shallow oceanic mixed-layer depths allow more rapid cooling of SSTs. The slab ocean model may be overly sensitive to the impact of anomalous surface fluxes on SST′ (primes denote departures from time mean) in regions of shallow oceanic mixed layer depths. As discussed in section 3, the OISST2 data product may not fully capture the actual SST variability. Because of its model configuration, no significant correlations or coherent patterns between precipitation and SST are noted in the CTL, as expected (Fig. 7b).

Figure 8 displays U850 lag correlated with 90°E precipitation. Implementation of the slab ocean model yields the largest improvement to the MJO in the Indian Ocean, where the CTL underestimates MJO convective intensity (Benedict and Randall 2009). For this reason, we focus on the MJO when it is convectively active in the Indian Ocean. The thick black line in Fig. 8 is the 5 m s^{-1} phase speed line. Observed patterns of U850 indicate a strong coupling of easterly followed by westerly anomalies as the maximum MJO rainfall passes. As convection moves into the central Pacific Ocean, it becomes decoupled from the dynamical signal and the MJO propagates as a faster, ''dry'' Kelvin wave into the Western Hemisphere as evidenced by the increased phase speed of the easterly–westerly couplet in Fig. 8 (compare to the 5 m s^{-1} phase speed line; Matthews 2000). Although the convective–dynamic coupling in both versions of the SP-CAM (Figs. 8b,c) is weaker than in nature, SOM has a longitudinally broader and more substantial couplet of leading easterlies and trailing westerlies. Specifically, the SOM results display a stronger signal of east Indian easterly anomalies, trailing westerlies that extend farther into the western Pacific, and a more developed

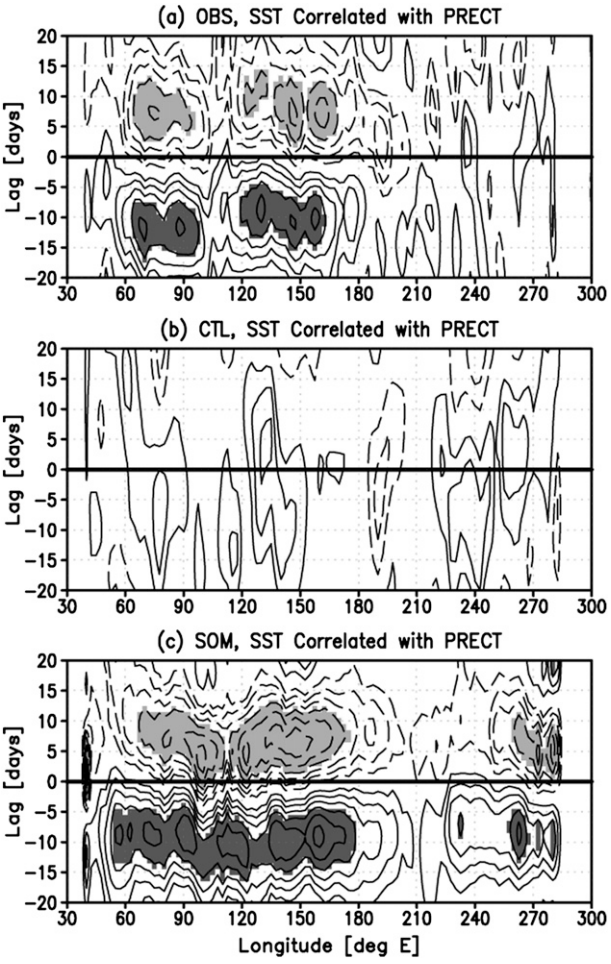

FIG. 7. SST lag correlated with precipitation for (a) observations, (b) CTL, and (c) SOM. Both fields are 20–100-day filtered and averaged between 10°S and 10°N. We use OISST2 and GPCP for the observed SST and precipitation fields, respectively. SST leads precipitation for negative lag days. Solid (dashed) contours indicate that precipitation and SST are positively (negatively) correlated. Light (dark) shading corresponds to regions in which correlations are statistically significant above the 95% level. Contour interval is 0.1; the zero contour is not drawn.

Kelvin wave signal in the central Pacific compared to CTL. Similar results are obtained for precipitation indices based at 120° and 150°E as well (not shown). Figure 8 suggests that a stronger, more coherent, and more longitudinally extensive relationship between MJO convection and dynamics is obtained when SSTs are allowed to ''respond'' to forcing from surface flux anomalies in the SP-CAM.

We use lagged linear regression analysis to depict the relationships among net surface flux, SST, and precipitation in the eastern Indian Ocean for ERAI, CTL, and SOM (Fig. 9). The net surface fluxes and SSTs are averaged between 10°S and 10°N and regressed onto the

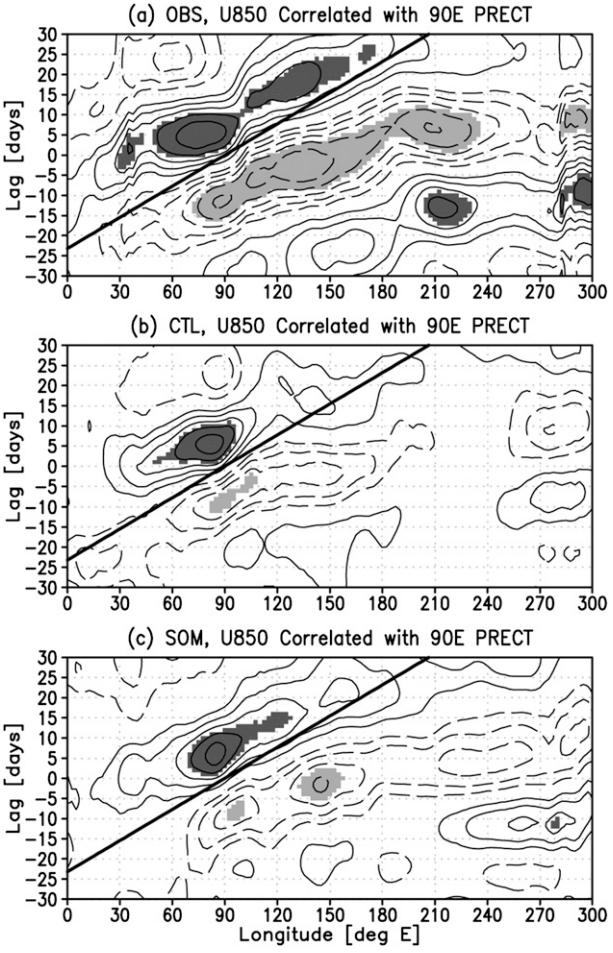

FIG. 8. Lag correlations of 850-hPa zonal wind with precipitation at 90°E for (a) observations, (b) CTL, and (c) SOM. Both fields are 20–100-day filtered and averaged between 10°S and 10°N. We use ERAI and GPCP for the observed wind and precipitation fields, respectively. The thick black line represents a 5 m s^{-1} phase speed. Contour intervals and significance shading are as in Fig. 7.

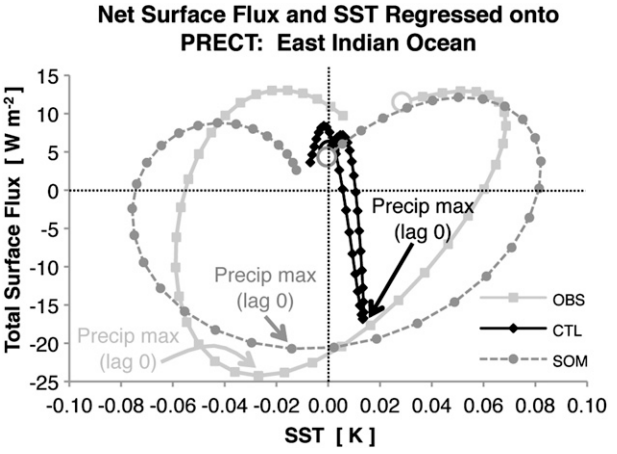

FIG. 9. Net surface flux and SST lag linearly regressed onto precipitation at 90°E for ERAI (light gray line), CTL (black line), and SOM (gray line). All fields are 20–100-day filtered and averaged between 10°S and 10°N, and the precipitation index has been standardized. Each dot represents a lag day relative to maximum precipitation (labeled) beginning with day −20, shown by a large open circle. Negative lags are days before heaviest rainfall. Positive flux values represent energy transfer into the ocean.

same precipitation index used in Fig. 8. For all regression plots in this paper, the fields are scaled to a one standard deviation change of the precipitation index. In Fig. 9, positive flux values represent energy transfer into the ocean, and each dot represents a lag day relative to maximum precipitation (labeled) beginning with day −20 (shown by a large open circle; negative lags represent days before heaviest rainfall). Although both SOM and CTL have realistic phasing between precipitation and net surface flux such that the strongest energy flux out of the ocean occurs near the time of maximum rainfall, large differences in the phasing of SST and net surface flux exist. In SOM, anomalies in SST lag those in net surface flux by 6–8 days, as seen in the reanalysis (light gray line of Fig. 9). SSTs and surface fluxes in CTL are nearly in phase, however. Shinoda et al. (1998) computed warm pool surface fluxes from gridded reanalyses to demonstrate that when intraseasonal SST fluctuations are removed from their flux calculations, the amplitude of intraseasonal surface evaporation increases. Consistent with their results, fluctuations of intraseasonal surface evaporation in SOM are weaker relative to CTL, although the difference is not substantial (not shown).

We display regression-based spatial patterns of the MJO time evolution in Figs. 10 and 11 . All variables have been averaged between 10°S and 10°N, and the regression index is again 90°E precipitation. Shaded areas (and emboldened wind vectors, for Fig. 10) are statistically significant above the 95% level. Figure 10 displays OLR, a proxy for deep convection, and 850-hPa vector winds regressed onto the 90°E precipitation index. Several key differences between CTL and SOM can be seen in Fig. 10. Prior to the peak in convective activity at 90°E (day −5, top), the CTL results show substantially weaker convection over the equatorial western Indian Ocean and Africa compared to either observations or SOM (Figs. 10a and 10c, respectively). This is consistent with the poor representation of deep convection propagating into the 90°E region from the west on earlier lag days (not shown). On day 0 (Fig. 10, middle) when precipitation peaks at 90°E near the equator, we note a broader and more realistic area of deep convection in SOM compared to CTL. More realistic patterns of convection and dynamics in SOM can also be seen on day +5 (Fig. 10, bottom). At this time, the SOM results (Fig. 10c) indicate a more robust development of

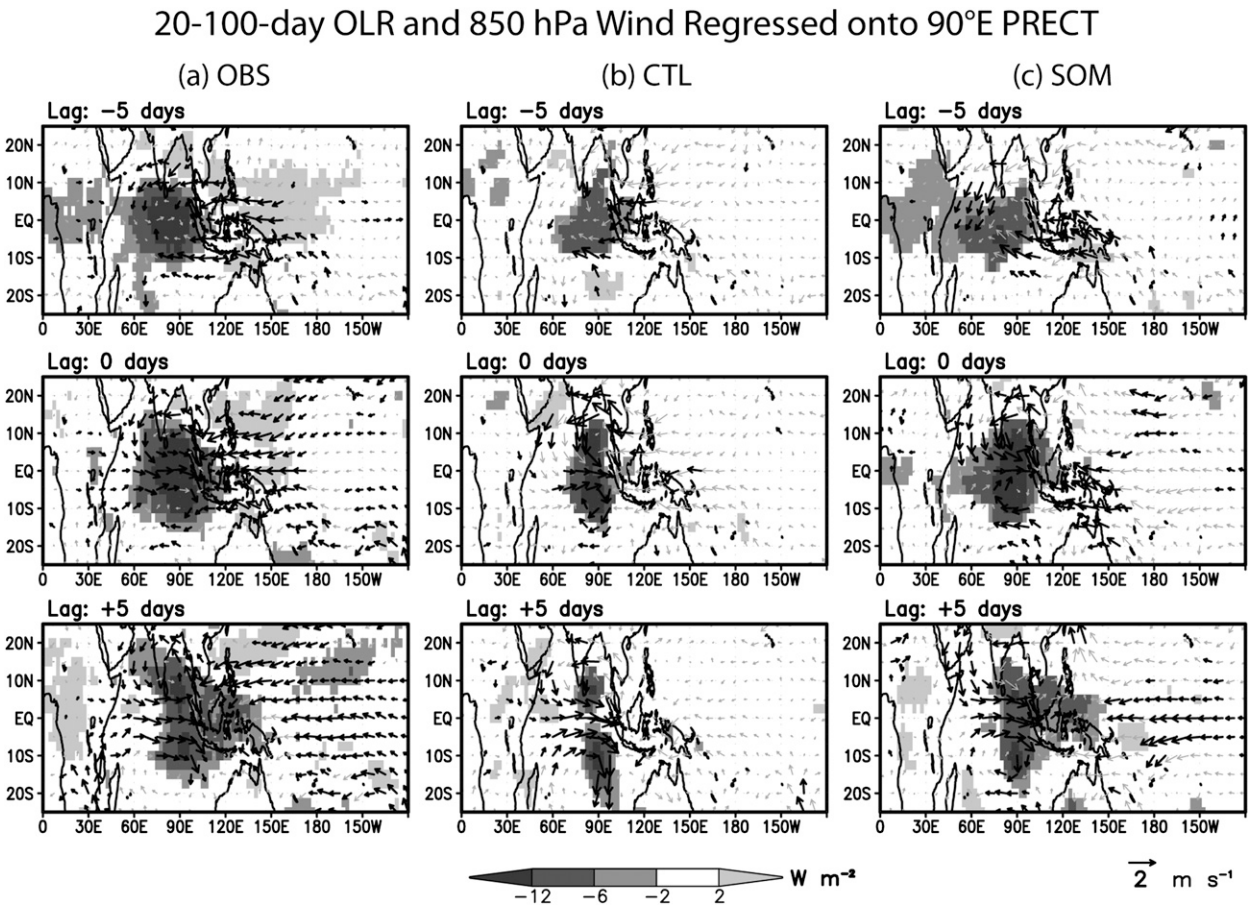

FIG. 10. OLR and 850-hPa zonal wind linearly regressed onto a precipitation index at 90°E for (a) observations, (b) CTL, and (c) SOM for (top to bottom) lags of −5, 0, and +5 days. All fields are 20–100-day filtered and averaged between 10°S and 10°N, and the precipitation index has been standardized. We use NOAA OLR, ERAI, and GPCP for observed OLR, wind, and precipitation fields, respectively. Regression magnitudes correspond to a one standard deviation change in the precipitation index. Wind vectors are thick where regression values are statistically significant above the 95% level, and OLR values are only shaded where they are significant. Negative lags represent days prior to the precipitation maximum at 90°E. Reference wind vector appears at the bottom right.

negative OLR anomalies over the Maritime Continent and significant equatorial 850-hPa easterly anomalies in the western and central Pacific compared to CTL (Fig. 10b). The CTL results (Fig. 10b, day +5) show that the main convective area is limited in longitude and is unrealistically weak along the equator. Additionally, western Pacific 850-hPa easterlies in the CTL are poorly developed at this time.

Lag regression patterns of surface pressure (Fig. 11) highlight important differences between the two versions of the SP-CAM. In nature (Fig. 11a), a surface pressure trough depicted by dashed contours has developed across the near-equatorial Indian Ocean on day −5. This trough evolves into a coupled Rossby–Kelvin wave structure, with robust Rossby gyres straddling the equator in the Indian Ocean and a broad Kelvin wave signal over the equatorial Pacific on day +5. The observed surface pressure trough that forms across the Indian Ocean about 1 week before deep convection initiates is not seen in the SP-CAM (Figs. 11b,c, top); rather, an area of low pressure develops in situ over the eastern Indian Ocean between days −5 and 0 (not shown). Between days 0 and +5, both versions of the SP-CAM form Rossby-like features in the Indian Ocean, but the off-equatorial centers of surface low pressure appear to be less distinct and shifted closer to the ~90°E heating center compared to the observed Rossby response in Fig. 11a. A clear Kelvin wave signal in the form of a surface pressure trough (Fig. 11c) and low-level easterlies (Fig. 10c) along the equator develops in SOM but not in CTL (Fig. 11b), consistent with the weak dynamical response seen in the 850-hPa wind field of CTL (Fig. 10b).

Lag regressions of additional variables, such as specific humidity and column-integrated moisture convergence (not shown), offer supporting evidence that the

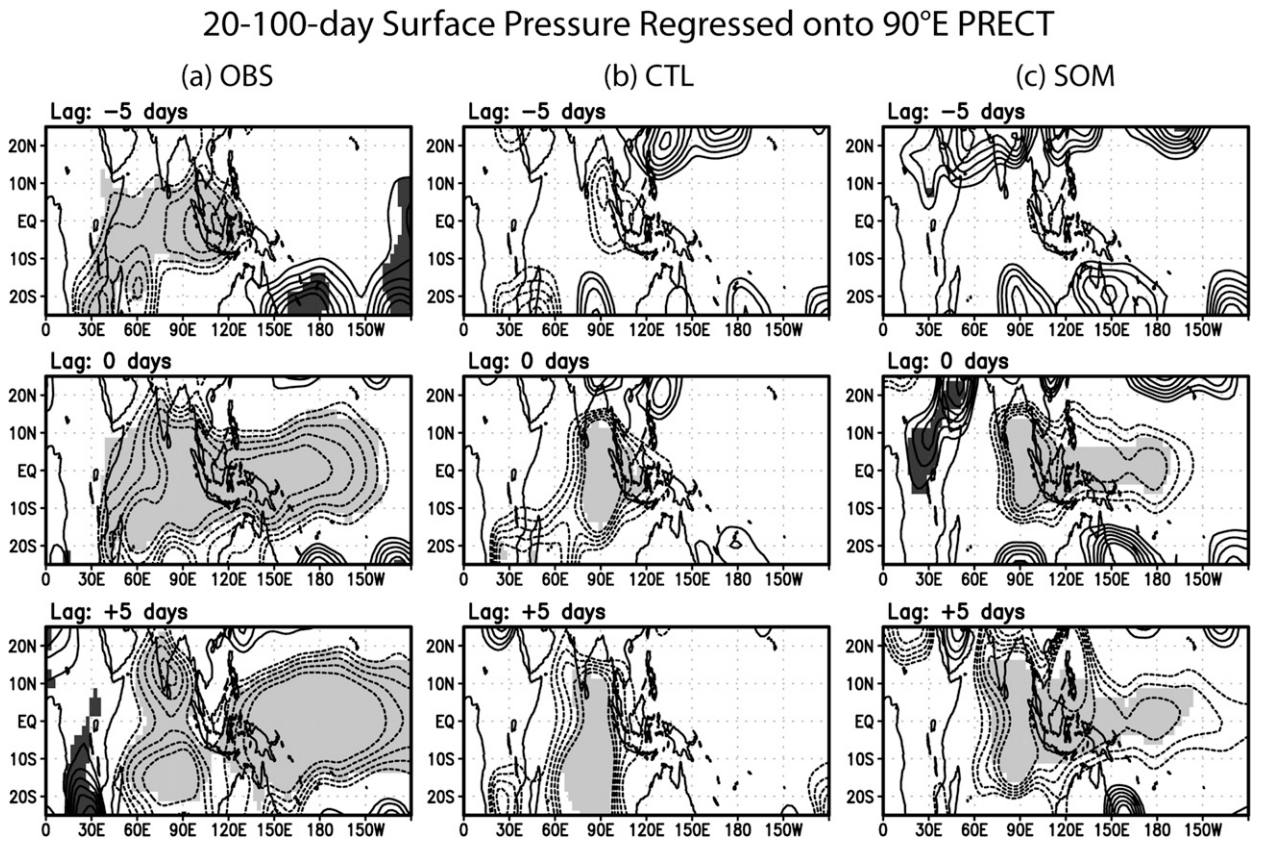

FIG. 11. Surface pressure linearly regressed onto a precipitation index at 90°E for (a) observations, (b) CTL, and (c) SOM for (top to bottom) lags of −5, 0, and +5 days. All fields are 20–100-day filtered and averaged between 10°S and 10°N, and the precipitation index has been standardized. We use ERAI and GPCP for observed surface pressure and precipitation fields, respectively. Regression magnitudes correspond to a one standard deviation change in the precipitation index. The contour interval is 5 Pa, and contouring begins at |15 Pa| and ends at |40 Pa|. Light (dark) shading represents areas where negative (positive) surface pressure values are statistically significant above the 95% level. Negative lags represent days prior to the precipitation maximum at 90°E.

SOM has a more realistic representation of MJO dynamic and thermodynamic processes than the CTL. This is particularly true when MJO convection is in the eastern Indian Ocean, where the CTL is known to underestimate MJO intensity (Benedict and Randall 2009). In the western Pacific, the SOM produces an improved MJO spatial structure compared to the CTL, but both models overestimate MJO intensity. Links between convergence, dynamical fields, and SSTs and their connection to the MJO simulated in the SP-CAM will be presented in section 6.

6. Discussion and conclusions

We have demonstrated that coupling the SP-CAM to a simplified slab ocean model results in significant changes to the simulated MJO. Results from the SOM suggest that coupling improves many aspects of tropical convection on intraseasonal time scales, from the fundamental relationships between intense precipitation and SSTs to the space–time structure and propagation of the MJO. We will now discuss mechanisms that may explain how the implementation of the slab ocean model in the SP-CAM leads to the MJO differences between the SOM and CTL.

To motivate our discussion, we present longitudinal profiles of numerous thermodynamic and dynamic variables in Figs. 12–15 . Selected variables are linearly regressed onto a standardized precipitation index time series at 90°E and then averaged within an equatorial band. To reduce the impact of coastal SST biases (see Fig. 1) and increase the number of oceanic points in the latitudinal sample, SSTs are averaged between 15°S and 5°N. We average all other variables between 5°S and 5°N and apply an 11-point running mean in longitude to reduce noise. Although there are areas of large MJO variance off the equator (see Figs. 2 and 3), this paper focuses mainly on mechanisms that affect MJO propagation in the zonal direction along the equator. The results and conclusions of this study are not highly sensitive to the choice of latitude range.

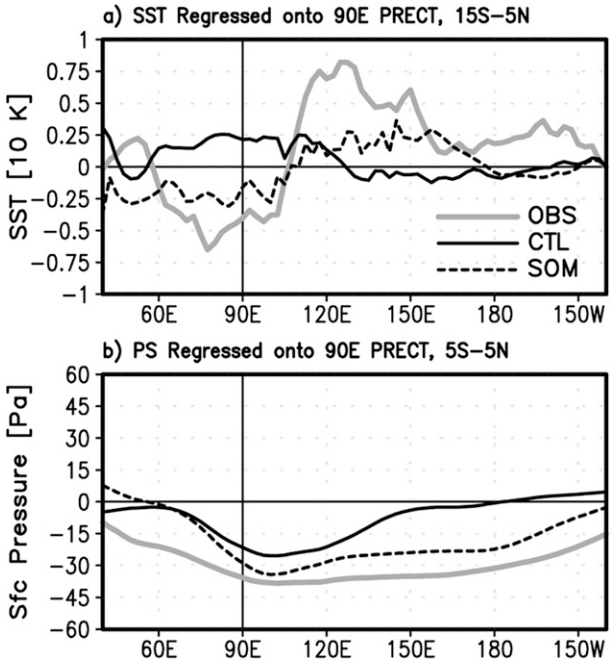

FIG. 12. Longitudinal cross sections of (a) SST and (b) surface pressure that have been linearly regressed onto a precipitation index at 90°E. Regressed SSTs (surface pressures) are latitudinally averaged between 15°S and 5°N (5°S and 5°N). We use OISST2 for the observed SST field, ERAI for observed surface pressure, and GPCP for observed precipitation. Regression magnitudes correspond to a one standard deviation change in the precipitation index at zero lag.

Figure 12 highlights lag-0 longitudinal profiles of regressed (a) SST and (b) surface pressure. Solid gray, solid black, and dashed black lines correspond respectively to observations, CTL, and SOM. In Fig. 12a, SST profiles reveal contrasting behavior between the SP-CAM simulations. In the uncoupled run, SST is roughly symmetric about the 90°E precipitation maximum, with almost no cooling of surface waters to the west of the MJO, and deep convection is longitudinally restricted to the region of highest SST (cf. Fig. 10). SST in the SOM is antisymmetric about 90°E, with warm surface waters to the east of the most intense convection and cooler SSTs within and to the west of the heavy precipitation region. SOM better captures the observed magnitude and structure of the zonal SST gradient when compared to CTL. The underestimated magnitude of SST fluctuations in SOM is likely related to its comparatively weaker equatorial net surface flux variance (see Fig. 4) or to limitations of the slab ocean model. The longitude–latitude behavior of lag-0 regressed SSTs (not shown) reveals that the largest positive SST anomalies are ~5°–10° off the equator for SOM, while anomalies along the equator are small. The largest SST anomalies in observations tend to be within 5° of the equator, especially across the western Pacific when peak MJO convection is at 90°E. This difference in SST spatial structure may be partly a result of the overestimation of equatorial convection in SOM (see Fig. 15). We also note that the phase relationships between variables that can influence SST in SOM—net surface longwave and shortwave radiation and latent and sensible heat fluxes—are qualitatively similar between the coupled and uncoupled runs (see Fig. 9). Because ocean surface temperatures cannot respond to surface flux anomalies in the uncoupled simulation, however, realistic zonal gradients of intraseasonal SST do not develop and this appears to negatively impact MJO representation in CTL.

In the Maritime Continent and western Pacific regions, perturbation surface pressures are lower in the SOM and are a closer match to observed profiles compared with CTL (Fig. 12b). In nature, minimum surface pressure anomalies coincide with maximum SST′ along the equator. In SOM, however, the largest SST perturbations in the western Pacific are just off the equator (not shown) while minimum surface pressures exist along the equator (Fig. 11a). We can infer that, when MJO deep convection is located at 90°E, the enhanced western Pacific equatorial trough in SOM arises primarily from dynamic contributions (improved representation of convective heating at 90°E and its related Kelvin wave response, as in Fig. 11c), with a smaller but nonnegligible effect from hydrostatic contributions (warmed ocean surface warms adjacent air and reduces surface pressure).

Given the enhancement of the low-level easterlies (Fig. 10) and equatorial surface pressure trough (Fig. 11) east of MJO deep convection in the SOM, we might expect a corresponding enhancement of lower tropospheric horizontal moisture convergence. Flux convergence of water vapor has been shown to play an important role in the maintenance and propagation of simulated and observed MJO disturbances (Wang and Xie 1998; Maloney and Hartmann 1998; Zhang et al. 2006). Figure 13 illustrates the structure of near-equatorial low-level convergence when MJO convection peaks at 90°E. All features noted in the discussions of Figs. 13–15 are statistically significant above the 95% level. Within the 600–850-hPa layer (Fig. 13a), moisture convergence in SOM is more robust and closer to observed values between 90° and 120°E. Figure 13c indicates that this enhancement of lower free-tropospheric convergence in SOM results primarily from the zonal mass convergence term $-r(\partial u/\partial x)$, where r is the mixing ratio of water vapor and nonprecipitating liquid. Within the 850–975-hPa layer, SOM and CTL moisture convergence profiles are similar with the exception of a stronger convergent signal in SOM between 130°E and 180°

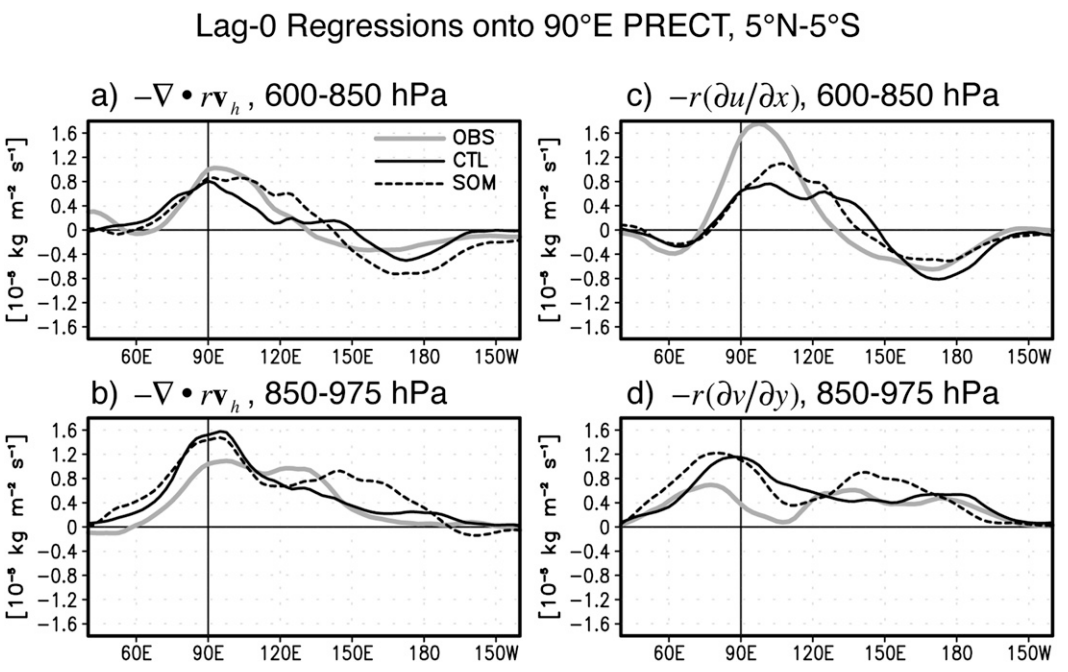

FIG. 13. As in Fig. 12, but for mass-weighted layer integrals of moisture convergence and its components. Profiles of total moisture convergence between (a) 600 and 850 hPa and (b) 850 and 975 hPa, (c) the zonal mass convergence component between 600 and 850 hPa, and (d) the meridional mass convergence component between 850 and 975 hPa are shown. Regression values are latitudinally averaged between 5°S and 5°N. In the panel titles, r is the mixing ratio of water vapor and nonprecipitating liquid and $\mathbf{v}_h$ is the horizontal wind vector.

(Fig. 13b). Figure 13d shows that this western Pacific increase is dominated by the meridional mass convergence term $-r(\partial v/\partial y)$. The area of increased boundary layer meridional convergence corresponds nicely to the region of lower surface pressures in SOM (Fig. 12b), strongly indicating that the frictional convergence mechanism (Wang 1988; Salby et al. 1994) is contributing to the MJO differences between SOM and CTL.

Along with the increase in lower tropospheric convergence east of MJO deep convection, SOM also shows larger positive anomalies of low-level moist static energy h compared to CTL. Figure 14 presents mass-weighted layer integrals of h regressed onto equatorial precipitation at 90°E. The largest h differences between CTL and SOM approximately correspond to areas with the largest moisture convergence differences (cf. Fig. 13): near 120°E for the 600–850-hPa layer and near 150°E in the 850–975-hPa layer. Importantly, the close association between increased h and meridional convergence within the boundary layer ahead of MJO deep convection lends further support to the hypothesis that the frictional convergence mechanism is more active in the SOM and is playing a role in the more organized MJO convection in that model. We note that the signal of increased boundary layer h ahead of MJO deep convection becomes much weaker both in models and in observations poleward of 10° from the equator (not shown).

The enhanced low-level h and convergence in SOM produce an environment that is more favorable for cumulus development as evidenced in Fig. 15, which displays longitudinal profiles of anomalous convective heating Q_1 [see (1) in Lin and Johnson 1996]. Cumulus heating is generally stronger in SOM compared to CTL, which results in an improvement to the heating signal in the eastern Indian Ocean but an overestimate in the western Pacific. Figure 15 also indicates that the westward-tilted structure of heating in the western Pacific is clearer in SOM compared to CTL. This SOM heating profile implies an increase in shallow cumulus activity ahead of deeper convective development, an MJO-related cloud structure that is prevalent in observations (Kikuchi and Takayabu 2004; Kiladis et al. 2005) and appears to play an important role in simulated MJO disturbances (Fu and Wang 2009).

The results of our analysis suggest the following MJO-related connection among SSTs, surface pressure, convergence, and convection in the coupled SP-CAM simulation. Although the phasing and magnitudes of surface flux anomalies relative to precipitation are similar between CTL and SOM, implementation of the slab ocean model in the coupled run produces a more realistic

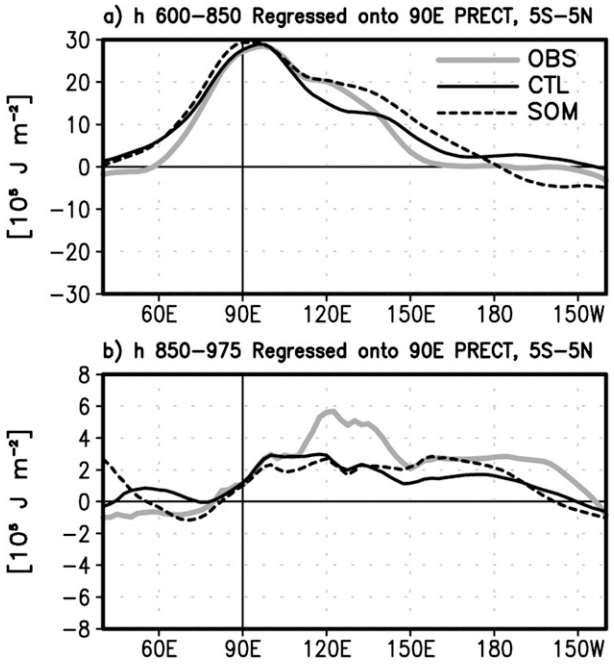

FIG. 14. As in Fig. 13, but for mass-weighted layer integrals of moist static energy h between (a) 600 and 850 hPa and (b) 850 and 975 hPa.

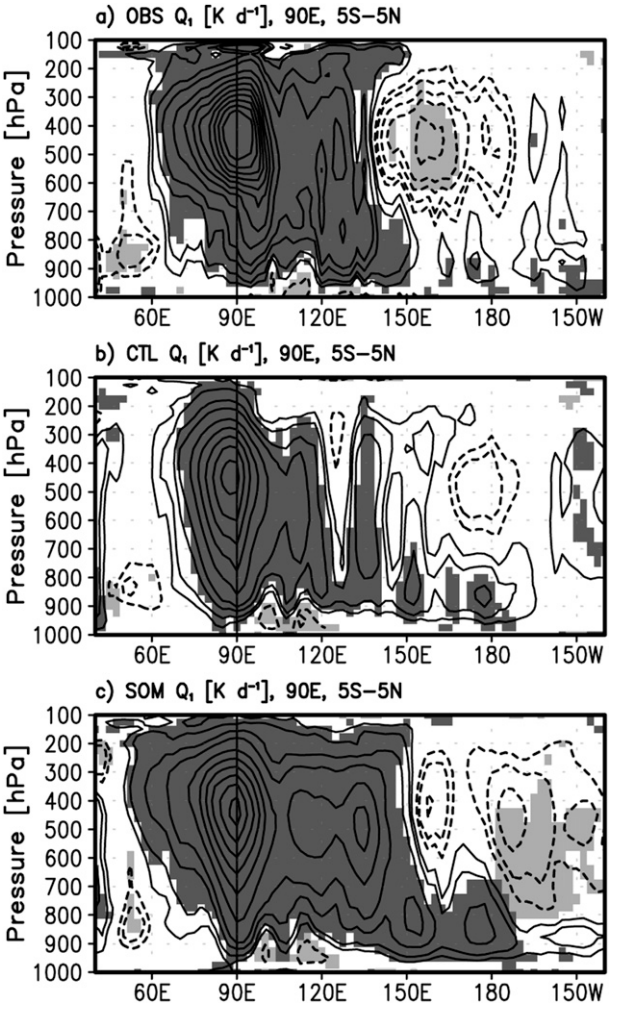

FIG. 15. Longitudinal cross sections of convective heating rate Q_1 linearly regressed onto a precipitation index at 90°E for (a) observations, (b) CTL, and (c) SOM. All fields are 20–100-day filtered and averaged between 5°S and 5°N. Solid (dashed) contours represent positive (negative) anomalies, which are darkly (lightly) shaded if they are statistically significant above the 95% level. The contour interval is 0.4 K day^{-1}, with the first contour ±0.2 K day^{-1}. The zero contour is not drawn.

longitudinal SST structure with warm surface temperatures leading the deep convective onset. When the MJO convective center is located at 90°E, the coupled SP-CAM produces a deeper equatorial surface pressure trough extending into the western Pacific. This area of lower surface pressure east of the convective center in the coupled SP-CAM is primarily a result of more vigorous Kelvin wave activity and, to a lesser extent, a hydrostatic reduction in surface pressure associated with larger positive SST′ just off the equator. Compared to the uncoupled SP-CAM, the coupled model produces two regions of heightened near-equatorial convergence, one over the Maritime Continent in the lower free troposphere (dominated by mass convergence in the zonal direction) and another across the western Pacific within the boundary layer (dominated by mass convergence in the meridional direction). In both of these strengthened convergence regions there are larger positive moist static energy anomalies. This combination of increased h' and stronger convergent flow promotes an environment that is more favorable for convective development ahead of the disturbance center and one that is shown to correspond to a more coherent transition from shallow cumuli to deep convection. In this way, a more robust MJO signal is obtained in the SOM relative to the CTL. The combination of strengthened boundary layer meridional convergence and a deeper equatorial surface pressure trough suggests that the frictional convergence mechanism (Wang 1988; Salby et al. 1994) is more active in the coupled SP-CAM and is a strong contributor to MJO differences between the two models.

We note a similar enhancement of MJO-related organization among convection, dynamics, and thermodynamics for regression profiles based at 60° and 120°E (not shown) in addition to the 90°E profiles discussed above. For example, when the MJO convective center is at 60°E, anomalous low-level convergence and SSTs at 90°E are substantially more positive in SOM relative to CTL (not show). This suggests that the improved MJO signal positively reinforces itself as the disturbance propagates eastward.

The paradigm we use to explain the improved MJO signal in the coupled SP-CAM shares some similarities with findings from previous studies that have examined air–sea coupling in traditional GCMs. Waliser et al. (1999) demonstrate that more realistic longitudinal SST gradients develop in their coupled model because of a positive cooperation between surface evaporation and insolation. In the present study, more realistic SST fields are noted in the SOM, but this improvement does not strongly correspond to more realistic longitudinal profiles of net surface fluxes, which drive SST fluctuations in the slab ocean model. Waliser et al. (1999) also show that positive SST′ leading deep convection supports low-level meridional moisture convergence and destabilization. Our results indicate that near-equatorial meridional moisture convergence leading MJO deep convection is primarily driven by a dynamically induced pressure trough and frictional convergence mechanism. Marshall et al. (2008) examine simulations of BAM3 and find that coupling results in a more realistic, warmer SST field east of MJO disturbances. The area of positive SST′ acts to offset MJO-induced weak evaporation, increase boundary layer warmth and moisture, hydrostatically reduce surface pressures, and ultimately drive enhanced low-level moisture convergence, which further elevates boundary layer moisture levels through deepening convection (Marshall et al. 2008). Our findings generally support the results of Marshall et al. (2008), although the deepened equatorial surface pressure trough in the coupled SP-CAM is related more to dynamical mechanisms rather than to hydrostatics.

While the findings discussed above and those from previous studies indicate that an improved simulation of the MJO in the CAM can be attained if a more realistic treatment of subgrid-scale processes and air–sea interactions is implemented (Benedict and Randall 2009; Zhu et al. 2009), there remain several areas of disagreement between the coupled SP-CAM results and observations. In regions of shallow oceanic mixed layer depths near landmasses, the sensitivity of SST′ to total surface flux anomalies is too strong (e.g., Fig. 1). We recommend that future simulations with the SP-CAM coupled to a slab ocean model increase the minimum allowable ocean mixed-layer depth to avoid this issue. Comparing SOM to observations, intraseasonal variability of U850 is unrealistically high in the tropics, and that of precipitation is too high (low) in the western Pacific (equatorial eastern Indian Ocean) region (Figs. 2 and 3). The signal-to-noise ratios of MJO and equatorial Rossby disturbances are too small in SOM (Fig. 6), and the coupling between convection and dynamics is unrealistically weak and spatially restricted (Fig. 8).

There are many factors that likely contribute to such inconsistencies in the SP-CAM, such as unrealistic convection–wind–evaporation feedbacks associated with the CRM's periodic boundary conditions in the SP framework (Luo and Stephens 2006), muted topography of Maritime Continent landmasses, and mean state biases (Benedict and Randall 2009). Additionally, the effects of convective momentum transport (CMT), which can have a considerable impact on large-scale wind fields (Mapes and Wu 2001) and the intensity and spatial distribution of precipitation (Khairoutdinov et al. 2005), are neglected in the two-dimensional CRM used in the present study. Yet another source of error in the SP-CAM may be the strong sensitivity of moisture in the lower boundary layer to surface evaporative fluxes. Benedict (2009) shows that lower boundary layer specific humidity anomalies were nearly in phase with surface latent heat flux anomalies during MJO disturbances in the both coupled and uncoupled versions of the SP-CAM. These biases appear to be linked to an underrepresentation of shallow cumuli and their attendant transport of moisture between the boundary layer and free troposphere within the CRM (Benedict 2009). That the SP-CAM still produces a realistic MJO despite the biases listed above underscores the importance of accurately representing subgrid-scale processes in GCMs.

This study is the first to examine in detail the impact of idealized air–sea coupling on the structure of the MJO in the SP-CAM, and the physical mechanisms associated with the observed changes. Our results strongly suggest that including a more realistic treatment of air–sea coupling, even if in an admittedly simple framework, produces a more organized relationship between convection and dynamics on intraseasonal space–time scales, and a more robust MJO signal. We have also demonstrated that although air–sea coupling has a positive impact on intraseasonal convective organization, it is not necessary for the existence of the MJO in the SP-CAM. Field campaigns such as Dynamics of the MJO (DYNAMO) and continued improvement of GCMs will advance our understanding of air–sea interactions and their role in the initiation and maintenance of the MJO.

Acknowledgments. We thank Z. Kuang and an anonymous reviewer for their helpful comments. We also thank Mark Branson for running the coupled SP-CAM simulation. This work was supported by the National Science Foundation Science and Technology Center for Multi-Scale Modeling of Atmospheric Processes (CMMAP), managed by Colorado State University under cooperative agreement ATM-0425247. J. B. has also been funded by award NA08OAR4320893 from the National Oceanic and Atmospheric Administration, U.S. Department of Commerce. The statements, findings, conclusions, and recommendations do not necessarily

reflect the views of NOAA or the Department of Commerce.

REFERENCES

Adler, R. F., and Coauthors, 2003: The version-2 Global Precipitation Climatology Project (GPCP) monthly precipitation analysis (1979–present). *J. Hydrometeor.,* **4,** 1147–1167.

Benedict, J. J., 2009: Structure of the Madden–Julian oscillation in coupled and uncoupled versions of the superparameterized Community Atmosphere Model. Ph.D. dissertation, Colorado State University, 194 pp.

——, and D. A. Randall, 2007: Observed characteristics of the MJO relative to maximum rainfall. *J. Atmos. Sci.,* **64,** 2332–2354.

——, and ——, 2009: Structure of the Madden–Julian oscillation in the superparameterized CAM. *J. Atmos. Sci.,* **66,** 3277–3296.

Berrisford, P., D. Dee, K. Fielding, M. Fuentes, P. Kallberg, S. Kobayashi, and S. Uppala, 2009: The ERA-Interim archive. ECMWF Tech. Rep. 1, 16 pp. [Available online at http://www.ecmwf.int/publications/library/do/references/show?id=89203.]

Bretherton, C. S., M. Widmann, V. P. Dymnikov, J. M. Wallace, and I. Bladé, 1999: The effective number of spatial degrees of freedom of a time-varying field. *J. Climate,* **12,** 1990–2009.

Chelton, D. B., and F. J. Wentz, 2005: Global microwave satellite observations of sea surface temperature for numerical weather prediction and climate research. *Bull. Amer. Meteor. Soc.,* **86,** 1097–1115.

Collins, W. D., and Coauthors, 2006: The formulation and atmospheric simulation of the Community Atmosphere Model version 3 (CAM3). *J. Climate,* **19,** 2144–2161.

DeMott, C. A., C. Stan, D. A. Randall, J. L. Kinter III, and M. Khairoutdinov, 2011: The Asian monsoon in the superparameterized CCSM and its relationship to tropical wave activity. *J. Climate,* in press.

Emanuel, K. A., 1987: An air–sea interaction model of intraseasonal oscillations in the tropics. *J. Atmos. Sci.,* **44,** 2324–2340.

——, 1994: *Atmospheric Convection*. Oxford University Press, 580 pp.

Flatau, M., P. J. Flatau, P. Phoebus, and P. P. Niiler, 1997: The feedback between equatorial convection and local radiative and evaporative processes: The implications for intraseasonal oscillations. *J. Atmos. Sci.,* **54,** 2373–2386.

Fu, X. H., and B. Wang, 2009: Critical roles of the stratiform rainfall in sustaining the Madden–Julian oscillation: GCM experiments. *J. Climate,* **22,** 3939–3959.

Hack, J. J., J. M. Caron, S. G. Yeager, K. W. Oleson, M. M. Holland, J. E. Truesdale, and P. J. Rasch, 2006: Simulation of the global hydrological cycle in the CCSM Community Atmosphere Model version 3 (CAM3): Mean features. *J. Climate,* **19,** 2199–2221.

Hayashi, Y., 1982: Space–time spectral analysis and its applications to atmospheric waves. *J. Meteor. Soc. Japan,* **60,** 156–171.

Hayes, S. P., L. J. Mangum, J. Picaut, A. Sumi, and K. Takeuchi, 1991: TOGA-TAO: A moored array for real-time measurements in the tropical Pacific Ocean. *Bull. Amer. Meteor. Soc.,* **72,** 339–347.

Hendon, H. H., 2005: Air–sea interaction. *Intraseasonal Variability in the Atmosphere–Ocean Climate System,* W. K. Lau and D. E. Waliser, Eds., Praxis-Springer, 223–246.

——, and M. L. Salby, 1994: The life cycle of the Madden–Julian oscillation. *J. Atmos. Sci.,* **51,** 2225–2237.

——, and J. Glick, 1997: Intraseasonal air–sea interaction in the tropical Indian and Pacific Oceans. *J. Climate,* **10,** 647–661.

Hu, Q., and D. A. Randall, 1994: Low-frequency oscillations in radiative–convective systems. *J. Atmos. Sci.,* **51,** 1089–1099.

Inness, P. M., and J. M. Slingo, 2003: Simulation of the Madden–Julian oscillation in a coupled general circulation model. Part I: Comparison with observations and an atmosphere-only GCM. *J. Climate,* **16,** 345–364.

Jones, C., and B. C. Weare, 1996: The role of low-level moisture convergence and ocean latent heat fluxes in the Madden and Julian oscillation: An observational analysis using ISCCP data and ECMWF analyses. *J. Climate,* **9,** 3086–3104.

Kawamura, R., 1988: Intraseasonal variability of sea surface temperature over the tropical western Pacific. *J. Meteor. Soc. Japan,* **66,** 1007–1012.

Kemball-Cook, S., B. Wang, and X. H. Fu, 2002: Simulation of the intraseasonal oscillation in the ECHAM-4 model: The impact of coupling with an ocean model. *J. Atmos. Sci.,* **59,** 1433–1453.

Khairoutdinov, M. F., and D. A. Randall, 2001: A cloud resolving model as a cloud parameterization in the NCAR Community Climate System Model: Preliminary results. *Geophys. Res. Lett.,* **28,** 3617–3620.

——, ——, and C. DeMott, 2005: Simulations of the atmospheric general circulation using a cloud-resolving model as a superparameterization of physical processes. *J. Atmos. Sci.,* **62,** 2136–2154.

——, C. DeMott, and D. Randall, 2008: Evaluation of the simulated interannual and subseasonal variability in an AMIP-style simulation using the CSU multiscale modeling framework. *J. Climate,* **21,** 413–431.

Kikuchi, K., and Y. N. Takayabu, 2004: The development of organized convection associated with the MJO during TOGA COARE IOP: Trimodal characteristics. *Geophys. Res. Lett.,* **31,** L10101, doi:10.1029/2004GL019601.

Kiladis, G. N., K. H. Straub, and P. T. Haertel, 2005: Zonal and vertical structure of the Madden–Julian oscillation. *J. Atmos. Sci.,* **62,** 2790–2809.

Kim, D., and Coauthors, 2009: Application of MJO simulation diagnostics to climate models. *J. Climate,* **22,** 6413–6436.

Krishnamurti, T. N., D. K. Oosterhof, and A. V. Mehta, 1988: Air–sea interaction on the time scale of 30 to 50 days. *J. Atmos. Sci.,* **45,** 1304–1322.

Lau, K.-M., and C.-H. Sui, 1997: Mechanisms of short-term sea surface temperature regulation: Observations during TOGA COARE. *J. Climate,* **10,** 465–472.

——, and D. Waliser, 2005: *Intraseasonal Variability in the Atmosphere–Ocean Climate System*. Springer-Praxis, 436 pp.

——, L. Peng, C. H. Sui, and T. Nakazawa, 1989: Dynamics of super cloud clusters, westerly wind bursts, 30–60-day oscillations, and ENSO: A unified view. *J. Meteor. Soc. Japan,* **67,** 205–219.

Liebmann, B., and C. A. Smith, 1996: Description of a complete (interpolated) outgoing longwave radiation dataset. *Bull. Amer. Meteor. Soc.,* **77,** 1275–1277.

Lin, J.-L., and Coauthors, 2006: Tropical intraseasonal variability in 14 IPCC AR4 climate models. Part I: Convective signals. *J. Climate,* **19,** 2665–2690.

Lin, X., and R. H. Johnson, 1996: Heating, moistening, and rainfall over the western Pacific warm pool during TOGA COARE. *J. Atmos. Sci.,* **53,** 3367–3383.

Luo, Z., and G. L. Stephens, 2006: An enhanced convection-wind-evaporation feedback in a superparameterization GCM (SP-GCM) depiction of the Asian summer monsoon. *Geophys. Res. Lett.,* **33,** L06707, doi:10.1029/2005GL025060.

Madden, R. A., and P. R. Julian, 1971: Detection of a 40–50-day oscillation in the zonal wind in the tropical Pacific. *J. Atmos. Sci.,* **28,** 702–708.

Maloney, E. D., and D. L. Hartmann, 1998: Frictional moisture convergence in a composite life cycle of the Madden–Julian oscillation. *J. Climate,* **11,** 2387–2403.

——, and A. H. Sobel, 2004: Surface fluxes and ocean coupling in the tropical intraseasonal oscillation. *J. Climate,* **17,** 4368–4386.

——, ——, and W. M. Hannah, 2010: Intraseasonal variability in an aquaplanet general circulation model. *J. Adv. Model. Earth Syst.,* **2** (5), doi:10.3894/JAMES.2010.2.5.

Mapes, B. E., and X. Q. Wu, 2001: Convective eddy momentum tendencies in long cloud-resolving model simulations. *J. Atmos. Sci.,* **58,** 517–526.

Marshall, A. G., O. Alves, and H. H. Hendon, 2008: An enhanced moisture convergence–evaporation feedback mechanism for MJO air–sea interaction. *J. Atmos. Sci.,* **65,** 970–986.

Matthews, A. J., 2000: Propagation mechanisms for the Madden–Julian oscillation. *Quart. J. Roy. Meteor. Soc.,* **126,** 2637–2651.

Monterey, G., and S. Levitus, 1997: *Seasonal Variability of Mixed Layer Depth for the World Ocean*. NOAA Atlas NESDIS 14, 96 pp.

Neelin, J. D., I. M. Held, and K. H. Cook, 1987: Evaporation–wind feedback and low-frequency variability in the tropical atmosphere. *J. Atmos. Sci.,* **44,** 2341–2348.

Rajendran, K., and A. Kitoh, 2006: Modulation of tropical intraseasonal oscillations by ocean–atmosphere coupling. *J. Climate,* **19,** 366–391.

Reynolds, R. W., N. A. Rayner, T. M. Smith, D. C. Stokes, and W. Wang, 2002: An improved in situ and satellite SST analysis for climate. *J. Climate,* **15,** 1609–1625.

Salby, M. L., R. R. Garcia, and H. H. Hendon, 1994: Planetary-scale circulations in the presence of climatological and wave-induced heating. *J. Atmos. Sci.,* **51,** 2344–2367.

Shinoda, T., H. H. Hendon, and J. Glick, 1998: Intraseasonal variability of surface fluxes and sea surface temperature in the tropical western Pacific and Indian Oceans. *J. Climate,* **11,** 1685–1702.

Simmons, A. J., S. Uppala, D. Dee, and S. Kobayashi, 2006: ERA-Interim: New ECMWF reanalysis products from 1989 onwards. ECMWF Newsletter, No.110, ECMWF, Reading, United Kingdom, 25–35. [Available online at http://www.ecmwf.int/publications/newsletters/pdf/110_rev.pdf.]

Slingo, J. M., and Coauthors, 1996: Intraseasonal oscillations in 15 atmospheric general circulation models: Results from an AMIP diagnostic subproject. *Climate Dyn.,* **12,** 325–357.

——, P. M. Inness, and K. R. Sperber, 2005: Modeling. *Intraseasonal Variability in the Atmosphere–Ocean Climate System,* W. K. Lau, and D. E. Waliser, Eds., Praxis-Springer, 361–388.

Sobel, A. H., E. D. Maloney, G. Bellon, and D. M. Frierson, 2008: The role of surface heat fluxes in tropical intraseasonal oscillations. *Nat. Geosci.,* **1,** 653–657.

Sperber, K. R., 2003: Propagation and the vertical structure of the Madden–Julian oscillation. *Mon. Wea. Rev.,* **131,** 3018–3037.

——, 2004: Madden–Julian variability in NCAR CAM2.0 and CCSM2.0. *Climate Dyn.,* **23,** 259–278.

——, S. Gualdi, S. Legutke, and V. Gayler, 2005: The Madden–Julian oscillation in ECHAM4 coupled and uncoupled general circulation models. *Climate Dyn.,* **25,** 117–140.

Stan, C., and Coauthors, 2010: An ocean–atmosphere climate simulation with an embedded cloud resolving model. *Geophys. Res. Lett.,* **37,** L01702, doi:10.1029/2009GL040822.

Straub, K. H., and G. N. Kiladis, 2003: The observed structure of convectively coupled Kelvin waves: Comparison with simple models of coupled wave instability. *J. Atmos. Sci.,* **60,** 1655–1668.

Thayer-Calder, K., and D. A. Randall, 2009: The role of convective moistening in the Madden–Julian oscillation. *J. Atmos. Sci.,* **66,** 3297–3312.

Uppala, S. M., and Coauthors, 2005: The ERA-40 Re-Analysis. *Quart. J. Roy. Meteor. Soc.,* **131,** 2961–3012.

Waliser, D. E., K. M. Lau, and J.-H. Kim, 1999: The influence of coupled sea surface temperatures on the Madden–Julian oscillation: A model perturbation experiment. *J. Atmos. Sci.,* **56,** 333–358.

Wang, B., 1988: Dynamics of tropical low-frequency waves: An analysis of the moist Kelvin wave. *J. Atmos. Sci.,* **45,** 2051–2065.

——, and X. Xie, 1998: Coupled modes of the warm pool climate system. Part I: The role of air–sea interaction in maintaining Madden–Julian oscillation. *J. Climate,* **11,** 2116–2135.

Webster, P. J., and R. Lukas, 1992: TOGA COARE—The Coupled Ocean–Atmosphere Response Experiment. *Bull. Amer. Meteor. Soc.,* **73,** 1377–1416.

Wheeler, M., and G. N. Kiladis, 1999: Convectively coupled equatorial waves: Analysis of clouds and temperature in the wavenumber–frequency domain. *J. Atmos. Sci.,* **56,** 374–399.

Zhang, C., 1996: Atmospheric intraseasonal variability at the surface in the tropical western Pacific Ocean. *J. Atmos. Sci.,* **53,** 739–758.

——, 2005: Madden–Julian oscillation. *Rev. Geophys.,* **43,** RG2003, doi:10.1029/2004RG000158.

——, and Coauthors, 2006: Simulations of the Madden–Julian oscillation in four pairs of coupled and uncoupled global models. *Climate Dyn.,* **27,** 573–592.

Zhang, G. J., and M. J. McPhaden, 1995: The relationship between sea surface temperature and latent heat flux in the equatorial Pacific. *J. Climate,* **8,** 589–605.

Zhu, H., H. Hendon, and C. Jakob, 2009: Convection in a parameterized and superparameterized model and its role in the representation of the MJO. *J. Atmos. Sci.,* **66,** 2796–2811.